

# Characterization and Evolution of Organized Shallow Convection in the Trades

Hauke Schulz<sup>1</sup>, Ryan M Eastman<sup>2</sup>, and Bjorn Stevens<sup>1</sup>

<sup>1</sup>Max Planck Institute for Meteorology

<sup>2</sup>U of Washington

November 24, 2022

## Abstract

Four previously identified patterns of meso-scale cloud organization in the trades – called Sugar, Gravel, Flowers and Fish – are studied using long-term records of ground-based measurements, satellite observations and reanalyses. A neural network trained to detect these patterns is applied to satellite imagery to identify periods during which a particular pattern is over the Barbados Cloud Observatory. Surface based remote sensing at the observatory is composited and shows that the patterns can be distinguished by differences in cloud macro-physical structures. Variations in total cloudiness among the patterns are dominated by variations in cloud-top cloudiness. Cloud amount near cloud base varies little. Each pattern is associated with a distinct atmospheric environment whose characteristics are traced back to origins that are not solely within the trades. Sugar air-masses are characterized by weak winds and of tropical origin. Fish are driven by convergence lines originating from synoptical disturbances. Gravel and Flowers are most native to the trades, but distinguish themselves with slightly stronger winds and stronger subsidence in the first case and greater stability in the latter. These results suggest that due to the tight bound of the patterns to wind and air-mass origin, the patterns with the higher cloud fraction, Flowers and Fish, will be disfavoured in a warming climate with more equable sea-surface temperatures and fewer mid-latitude disturbances.



## 10 **Abstract**

11 Four previously identified patterns of meso-scale cloud organization in the trades – called  
 12 *Sugar*, *Gravel*, *Flowers* and *Fish*– are studied using long-term records of ground-based  
 13 measurements, satellite observations and reanalyses. A neural network trained to detect  
 14 these patterns is applied to satellite imagery to identify periods during which a partic-  
 15 ular pattern is over the Barbados Cloud Observatory. Surface based remote sensing at  
 16 the observatory is composited and shows that the patterns can be distinguished by dif-  
 17 ferences in cloud macro-physical structures. Variations in total cloudiness among the pat-  
 18 terns are dominated by variations in cloud-top cloudiness. Cloud amount near cloud base  
 19 varies little. Each pattern is associated with a distinct atmospheric environment whose  
 20 characteristics are traced back to origins that are not solely within the trades. *Sugar* air-  
 21 masses are characterized by weak winds and of tropical origin. *Fish* are driven by con-  
 22 vergence lines originating from synoptical disturbances. *Gravel* and *Flowers* are most  
 23 native to the trades, but distinguish themselves with slightly stronger winds and stronger  
 24 subsidence in the first case and greater stability in the latter. These results suggest that  
 25 due to the tight bound of the patterns to wind and air-mass origin, the patterns with  
 26 the higher cloud fraction, *Flowers* and *Fish*, will be disfavoured in a warming climate  
 27 with more equable sea-surface temperatures and fewer mid-latitudinal disturbances.

## 28 **1 Introduction**

29 The organization of deep convection has long been recognized to influence the dis-  
 30 tribution of moisture and as a consequence the climate. Shallow convection, as is com-  
 31 mon in the trades for instance, is usually not thought of being organized. Rather, in the  
 32 mind’s eye of many researchers, trade-wind clouds were randomly distributed have lit-  
 33 tle vertical development and their role in the climate system was, at best, taken for granted  
 34 in early studies. Over the past twenty years however, the out-sized role of maritime shal-  
 35 low convection on Earth’s radiation budget and discrepancies in how models predict their  
 36 changes with warming (Bony & Dufresne, 2005), have made a determination of processes  
 37 controlling their coverage a central focus of climate science. During this period, obser-  
 38 vational studies such as RICO (Rauber et al., 2007) and the emergence of satellite im-  
 39 agery with spatial resolution on the hecta-meter scale began emphasizing how shallow  
 40 clouds in the trades adopt different forms of organization, often in association with pre-  
 41 cipitation development and the formation of cold pools (Zuidema et al., 2012; Seifert &

42 Heus, 2013; Seifert et al., 2015). More recently, studies have shown that shallow convec-  
43 tion can be categorized into several (four) large scale patterns (Stevens et al., 2020) and  
44 the form of organization influences the net cloud radiative effects and thus may influ-  
45 ence Earth’s climate sensitivity (Bony et al., 2020).

46 As reviewed by Nuijens, Louise and Jakob, Christian (2020), the classification of  
47 clouds into types and patterns has a long tradition. Categorization and classification help  
48 to break a complex problem down, into more manageable pieces, and thereby help to nav-  
49 igate nature’s complexity in ways that open it to our understanding and perception. In  
50 contrast to classifications based on particular cloud types, as defined in the *International*  
51 *Cloud Atlas* (WMO, 2017), or to classifications based on mean properties, recent work  
52 has emphasized the large-scale patterns defined by the tiling of mesoscale elements as  
53 a basis for categorizing trade-wind cloud regimes (Stevens et al., 2020), similar to what  
54 has been done in the past to characterize cloud fields forming in association with cold-  
55 air outbreaks, or over land, or in regions where stratocumulus clouds predominate (Agee,  
56 1987; Atkinson B. W. & Wu Zhang J., 1996; Young et al., 2002).

57 Following this tradition, Stevens et al. (2020) identified four patterns – which they  
58 called *Sugar*, *Gravel*, *Flowers* and *Fish*– based purely on visual satellite imagery in the  
59 vicinity of the Barbados Cloud Observatory. Of these only *Sugar* fit the prevailing view  
60 of the trades being covered by random dustings of cumulus humilis atop the background  
61 of a dark ocean. A follow-up study by Rasp et al. (2020) showed that these four patterns  
62 can be identified not only in the region of the North-Atlantic trades studied by Stevens  
63 et al. (2020), but they form in trade-wind regimes in every ocean basin. As mentioned  
64 above, the four patterns also differ in their net cloud radiative effects. This raises the  
65 question as to whether in a warmer climate, changes in cloudiness might be manifested  
66 by a different balance in their form of organization (Bony et al., 2020).

67 Motivated by the potential impact on climate sensitivity and the striking differ-  
68 ences in the visual appearance of the four patterns identified by Stevens et al. (2020),  
69 we are interested in better understanding the basic features of these four patterns, and  
70 the factors that influence their emergence. More specifically, we aim to answer the ques-  
71 tions:

- 72 1. How do the four patterns differ in terms of the observed cloud macro-physical prop-  
73 erties?

- 74           2. Are the different patterns associated with different large-scale environments.  
75           3. To what extent are these large-scale differences reflective of different air mass ori-  
76           gins?

77           To answer these questions we collocate the four cloud patterns of meso-scale or-  
78           ganization as automatically detected in satellite measurements with observations made  
79           at the Barbados Cloud Observatory. This contextualization of the high-resolution ground-  
80           based cloud measurements within the meso-scale patterning enables us to get deeper in-  
81           sights about their characteristics in ways that are not possible using satellite measure-  
82           ments alone.

83           The methods adopted and the data used are described in Section 2. A character-  
84           ization of the cloud patterns with a focus on the macro-physical properties and how it  
85           fits with our preconceptions as derived from the satellite images is given in Section 3.  
86           Further, we analyse in Section 4 the meteorological conditions under which the patterns  
87           occur and the extent to which they can be distinguished. Finally, we address the ques-  
88           tion about the evolution of the air masses giving rise to the patterns by using back-trajectories,  
89           analyzing the seasonal distribution and synoptic (large-scale weather patterns) influences  
90           in Section 5. We conclude with Section 6.

## 91   **2 Method**

### 92    **2.1 Pattern detection of shallow convection**

93           A crucial part of this study is the detection of the four patterns of shallow convec-  
94           tion. We base our approach on the neural network architecture described in Rasp et al.  
95           (2020), which has been trained with 10 000 manually labeled satellite images. While these  
96           manual classifications were performed for 10 years of visible imagery captured by the Mod-  
97           erate Resolution Imaging Spectroradiometer (MODIS) instruments aboard the satellites  
98           AQUA and TERRA, the neural network used in this study is trained with the infrared  
99           counterpart. Use of the infrared imagery was adopted to capture the patterns on a sub-  
100          daily time-scale as they do not necessarily preserve their organization throughout the  
101          day. Using infrared data lets us apply the neural network on the infrared images cap-  
102          tured at night, but also at much higher frequency using measurements from the geosta-  
103          tionary satellite GOES16. While the GOES16 Advanced Baseline imager can capture  
104          images every minute for pre-selected regions, here we use only the brightness temper-

105 atures in the clean infrared long-wave window (channel 13; 10.46  $\mu\text{m}$ ) at a temporal res-  
 106 olution of 30 minutes.

107 The training of the neural network in the infrared is straight forward. Instead of  
 108 using the visible images during training, the infrared imagery has been used while keep-  
 109 ing the manual classifications the same as if the classifications were made on the infrared  
 110 imagery. The mean pixel agreement between the infrared and visible neural network clas-  
 111 sifications for AQUA daylight overpasses on the north Atlantic domain used in Rasp et  
 112 al. (2020) is 0.4, 0.5, 0.5, 0.2 for *Sugar*, *Gravel*, *Flowers*, and *Fish*, respectively. The to  
 113 some degree lower agreement in case of *Fish* can mostly be attributed to the cloud-top  
 114 height information that the infrared neural network uses to reduce false classifications  
 115 of cirrus clouds that occasionally can be a carbon copy of *Fish*.

116 To attribute one of the four patterns to the observations made at the Barbados Cloud  
 117 Observatory, each classification of the neural network is evaluated at the location of the  
 118 observatory. Because the site can be at the edge of a classification and we wish to in-  
 119 clude only clear and long-lasting patterns, a 6 h time period is associated with a specific  
 120 pattern if for at least half of the time (3 h) a specific pattern prevails. The three win-  
 121 ter seasons (November through March) 2018-2020 during which GOES16 data, with its  
 122 higher-resolution infrared imager, are available are used for our analysis. Because the  
 123 patterns occur not equally likely, the number of detected cases differs as indicated in Tab. 1,  
 124 with 42% of the 6 h windows being associated with one of the four patterns. The remain-  
 125 ing periods were grouped together as *Others*.

**Table 1.** Number of time windows that contain robustly identified patterns in the winters of 2018 (JFM), 2019 (NDJFM) and 2020 (NDJFM)

pattern	# of 6h windows	% of total
Sugar	125	9
Gravel	282	19
Flowers	77	5
Fish	138	9
Others	846	58

126 For the detection of the seasonal cycle of the patterns and the trajectory analysis  
127 we use a different approach. First, because the GOES16 Advanced Baseline Imager does  
128 not cover the complete North Atlantic, we base this part of the analysis on the patterns  
129 detected in images captured by MODIS during daytime AQUA overpasses. Second, be-  
130 cause this analysis is based on MODIS the longer time-record of AQUA can be used to  
131 improve the sampling. For this purpose we use the 10 year period between 2010 and 2020  
132 inclusive.

## 133 **2.2 Back-trajectories**

134 To analyze the origin of the patterns and the evolution of the air mass in which they  
135 are found, we calculate back-trajectories following the framework of Eastman and Wood  
136 (2016). Vertical winds are assumed to be negligible compared to the horizontal compo-  
137 nents, such that the trajectories are followed near the top of the sub-cloud (boundary)  
138 layer and kept constant at the initial height of 925 hPa. These boundary-layer trajec-  
139 tories are calculated using winds from the 5th European Center Reanalysis of meteoro-  
140 logical observations (ERA5) (Hersbach et al., 2020) on a 6-hourly time step.

141 The back-trajectories are initialized at the center of each classification within the  
142 domain  $10^{\circ}\text{N}$ - $24^{\circ}\text{N}$  and  $61^{\circ}\text{W}$ - $40^{\circ}\text{W}$  and most closely to the AQUA overpass time. The  
143 analysis covers the winter months (November through March) of 2010-2020. Trajecto-  
144 ries are calculated for an 84 h period and atmospheric properties along the trajectory are  
145 extracted at each 12-hour time-step coinciding with a MODIS Aqua overpass. Reanal-  
146 ysis variables are taken from a  $1\times 1$  degree latitude-longitude grid, with averages produced  
147 for all boxes with centers that fall within 100 km of trajectory sampling points.

## 148 **2.3 Surface observations**

149 Surface observations in the trades, where these meso-scale patterns occur, are sparse,  
150 especially those beyond standard meteorological reports from ships and buoys. The Bar-  
151 bados Cloud Observatory (BCO) is one exception and studies have shown that the at-  
152 mosphere it samples at the most windward tip of Barbados is representative for the mar-  
153 itime conditions in the downwind trades more generally (Stevens et al., 2016; Medeiros  
154 & Nuijens, 2016).

155 The BCO uses advanced remote sensing instrumentation to measure the undisturbed  
156 marine subtropical atmosphere (Stevens et al., 2016). In this study, we use simultane-  
157 ous measurements from the CORAL Ka-band cloud radar and Raman lidar to charac-  
158 terize clouds and their thermodynamic environment, especially the surrounding humid-  
159 ity structure of the clouds. These advanced remote-sensing measurements are comple-  
160 mented by soundings of the nearby Grantley-Adams airport to improve the statistics above  
161 clouds, which can quickly attenuate the lidar signal and make a retrieval inside and above  
162 clouds impossible. Radiosondes are launched once or twice a day, usually an hour or so  
163 of their 0 UTC and 12 UTC report times.

164 To detect only hydro-meteors with the cloud radar and no sea-salt aerosols, we ap-  
165 ply a threshold of  $-50$  dBZ as used in Klingebiel et al. (2019).

166 In addition to the standard surface meteorological measurements from a Vaisala  
167 WXT-520, we use the rain rate measurements from a micro-rain radar (MRR). Due to  
168 its larger sampling area compared to the also available acoustic rain sensor, it detects  
169 more reliable light and/or short rain events. However, this comes at the cost of measur-  
170 ing the rain rate above the surface (325 m) rather than at the surface – which likely over-  
171 estimates rain amount, particularly for light rain.

## 172 **2.4 Cloud entity classification**

173 The identifications of meso-scale patterns of shallow convection are supplemented  
174 with cloud-type classifications derived from the BCO measurements.

175 Macro-physical properties of clouds down to single cloud entities are retrieved based  
176 on the segmentation of the radar reflectivity. Individual clouds are identified by testing  
177 the connectivity of radar retrievals in height and time. Since a main part of this study  
178 focuses on stratiform layers, we use a running window of 100 s in time and only direct  
179 connections in the vertical to account for the fact, that the stratiform layers can be so  
180 thin that they are not continuously detected by the radar. To exclude false classifica-  
181 tions as much as possible due to slanted cumulus clouds that can be falsely detected as  
182 stratiform clouds, we consider only clouds with a pass time of 2 min or more for the cloud  
183 entity analysis.

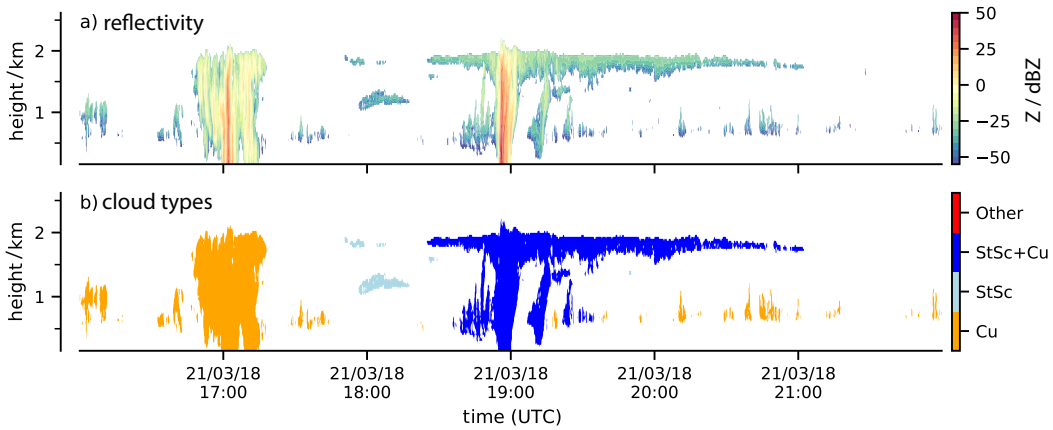


**Figure 1.** Example of cloud-type classification based on radar reflectivity

184 Similar to Lamer et al. (2015) we classify individual clouds by their cloud base heights  
 185 (CBH). Stratiform layers are defined as clouds that have a frequent CBH above 1 km up  
 186 to 2.5 km. If the CBH is in general below 1 km the cloud is classified as originating from  
 187 the cumulus gene. An example of the radar reflectivity and the derived cloud-type clas-  
 188 sifications is shown in Fig. 1. It illustrates, that also a mixture of cumulus with an at-  
 189 tached stratiform layer may exist. These cases are actually classified as “StSc+Cu” in  
 190 the case the stratiform layer exists for at least 20 % within a cumulus cloud-entity.

191 Based on the single cloud entities the macro-physical properties like stratiform ex-  
 192 tent, rain flag and the mean thickness of the stratiform layer are calculated and asso-  
 193 ciated with each entity.

### 194 **3 Surface based characterization of cloudiness and precipitation**

195 The four patterns identified by Stevens et al. (2020) – *Sugar*, *Gravel*, *Flowers*, *Fish*–  
 196 are purely defined by their visual impression from space, predominantly the spatial dis-  
 197 tribution of cloudiness. The cloudiness is therefore the closest physical quantity to the  
 198 subjective definition of these patterns. Among the physical differences that may accom-  
 199 pany these patterns, aspects of cloudiness that go beyond the spatial arrangement of re-  
 200 flectivity as seen from above will be important to characterize, especially in so far as it  
 201 influences the cloud radiative effect.

202 An overview of these patterns and the ground based observations linked to them  
 203 is shown in Fig. 2. Differences in cloudiness are readily apparent, and conform to what

204 has been previously noted in the literature. *Sugar* is identified with a fine dusting of clouds,  
 205 *Gravel* with cloud features arranged around arc-like structures. *Flowers* and *Fish* are  
 206 composed of elements that are yet larger in scale and show a clearer separation between  
 207 cloudy and clear-sky areas. For *Flowers* the clouds show a more isotropic distribution,  
 208 while they are usually elongated – roughly West to East – in the case of *Fish*.

209 From these illustrations, which add to the examples shown in Stevens et al. (2020),  
 210 it is natural to develop preconceptions about differences in the three dimensional struc-  
 211 ture of the boundary layer associated with the patterns. For example, *Gravel* is gener-  
 212 ally thought to be associated with precipitation due to the visible cold pool signature  
 213 in the cloud field, and *Flowers* are thought to be composed of stratiform clouds with sup-  
 214 pressed convection around them. Assessing whether such preconceptions are supported  
 215 by the data, rather than manifestations of extreme and unrepresentative cases, is one  
 216 of the goals of this section.

217 We first focus on the characteristics of the cloudiness in terms of their macro-physical  
 218 and geometric properties. Thereafter we analyse the precipitation signatures of the pat-  
 219 terns, as they might help to gain a process understanding on how these different patterns  
 220 form.

### 221 3.1 Cloudiness

222 The cloud cover at the Barbados Cloud Observatory is shaped by the ubiquitous  
 223 appearance of cumulus humilis – i.e., cumulus clouds of very limited vertical extent. Cu-  
 224 mulus humilis are not the only cloud type measured at the site. Even in the northern  
 225 hemispheric winter, when the Intertropical Convergence Zone is furthest away from Bar-  
 226 bados and the region experiences strong subsidence, the measured cloud fraction is not  
 227 solely caused by non-precipitating cumulus humilis. This is demonstrated by an anal-  
 228 ysis of the mean echo fraction profile ( a combination of cloud- and rain-fraction) shown  
 229 in Fig. 3. Echoes are detected extending to depths above 3 km.

230 Looking at the mean echo fraction profiles of *Sugar*, *Gravel*, *Flowers* and *Fish* and  
 231 also the overall wintertime mean echo fraction, suggests that all but *Fish* are some breed  
 232 of shallow convection, with very small echo fractions (less than 3% at 4 km) extending  
 233 much above 2.5 km. *Fish* appears distinct. Its echo fraction is larger than the seasonal

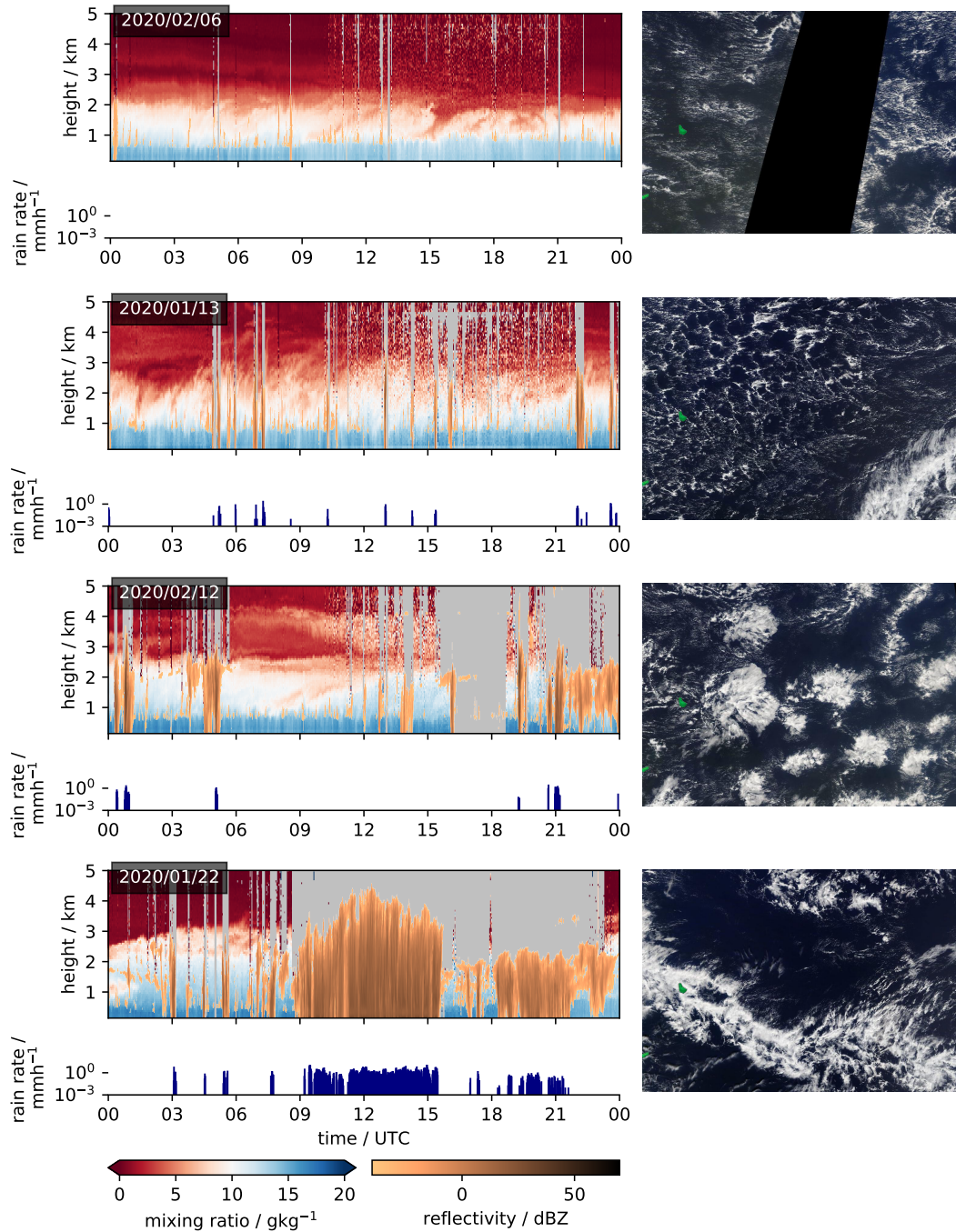


**Figure 2.** Time-series of each cloud pattern as identified by scientists participating in the EUREC<sup>4</sup>A campaign (top to bottom: *Sugar*, *Gravel*, *Flowers*, *Fish*). Water vapor measurements from the Raman lidar overlaid by radar reflectivity shown in upper panels, while rain rates measured at 325 m are shown in the lower panels. The according MODIS images from the TERRA satellite overpass are shown on the right. Missing values are colored grey.

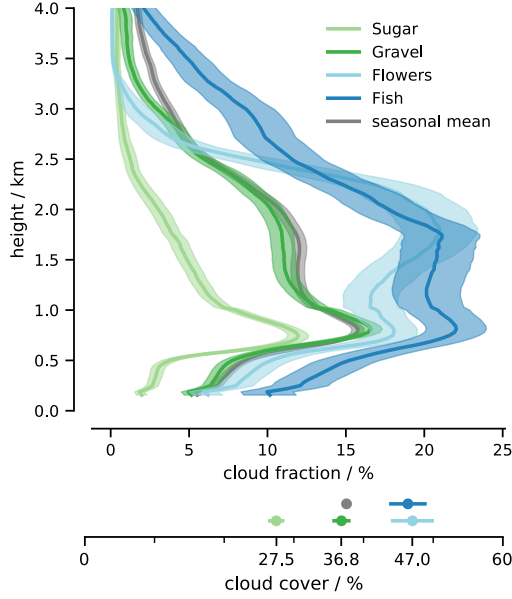


**Figure 3.** Echo-fraction measured at the Barbados Cloud Observatory and grouped by detected pattern indicating the combination of cloud- and rain-fraction (upper panel). The height integral, echo coverage, is shown in the bottom panel. The overall mean of the analysed winter seasons is shown in grey. Shading indicates standard error of mean.

234 mean, also above the moist cloud-layer usually identified with the region below the maxi-  
 235 mum echo-fraction between 2.0 km to 2.5 km.

236 Differences near the lifting condensation level (i.e., associated with a local maxi-  
 237 mum in the echo fraction near 750 m) are less pronounced. Here, independent of the cloud  
 238 pattern, and more general independent of any observed cloud distribution, echo fractions  
 239 are more similar. The lack of variability of cloud amount at the cloud-base height was  
 240 emphasized by Nuijens et al. (2014). The variations that exist can largely be attributed  
 241 to rain events, i.e., differences below 500 m – which are a signature of precipitation – are  
 242 similar to those at 700 m. This implies that the non-raining cloud-base echo fraction dif-  
 243 fers little among the patterns and is similar to the seasonal mean. That *Flowers* would  
 244 have a similar echo fraction at cloud-base after the rain correction as *Sugar* was not some-  
 245 thing we would have guessed from the satellite imagery. It shows that an abundance of  
 246 clouds near cloud-base under the cloud shield compensates for an absence of shallow-cloudiness  
 247 in the cloud-free part of the *Flowers* pattern.

248 Fig. 3 further suggests that cloudiness aloft, in the layer between 1.5 km to 2.5 km,  
 249 explains a large part of the differences in the satellite imagery which gives rise to the dif-  
 250 ferent patterns. For instance *Flowers*, with its cloudy patches of high reflectivity paired  
 251 with the sheet-like structure anticipate a strong stratiform component in the cloud frac-  
 252 tion compared to *Sugar* and *Gravel*, as is indeed evident in the echo-fraction profiles.  
 253 *Fish* has high echo-fractions throughout the cloud layer, but are less obviously dominated  
 254 by a stratiform component as compared to simply more cloudiness, which often extends  
 255 much more deeply through the lower troposphere. In the case of *Gravel*, a local max-  
 256 imum in cloudiness aloft is hardly evident and completely missing for *Sugar*. It is there-  
 257 fore the cloudiness aloft, that varies most with about 15 % at 1.7 km and distinguishes  
 258 the cloud fraction profiles of the patterns.

259 Looking at the cloudiness of the patterns as a whole, we recognize, that the echo  
 260 fraction of *Gravel* has the strongest similarity to the seasonal mean echo fraction, which  
 261 is the average of all 6 h windows independent of any pattern. This is consistent with *Gravel*  
 262 being the most common pattern detected in this study (about 19 % of all regarded time  
 263 windows and 45 % of the windows with any dominant pattern). Further, it also suggests,  
 264 that a large portion of the more uncertain and mixed time-windows contains cloudiness  
 265 similar to the *Gravel* pattern. *Sugar*, in contrast, occurs rather more seldom. This might  
 266 seem to contradict Rasp et al. (2020) who found that *Sugar* is actually more often iden-  
 267 tified than *Gravel*. However, similar to Stevens et al. (2020), who were looking for dom-  
 268 inating patterns on a fixed domain, we look for dominating patterns within a fixed time-  
 269 period. Both methods register only patterns that are persistent for a long time or cover  
 270 a large area, both of which de-emphasize *Sugar*. The cloud pattern with randomly dis-  
 271 tributed clouds of little vertical extent occurs frequently, but is often not dominant and  
 272 thus not picked out by our analysis.

273 In the following, we decompose the cloudiness further into individual cloud enti-  
 274 ties. Each of those cloud entities is then classified, as described in Sec. 2.4, into the tra-  
 275 ditional cloud genes: cumulus, stratus, or as a combination of those in case they are con-  
 276 nected. This way, we analyze whether the patterning has an influence on the distribu-  
 277 tion, frequency and composition of cloud types. For instance, based on the above, one  
 278 would immediately expect stratiform clouds to dominate for *Flowers* and be absent for  
 279 *Sugar*.

280 The entity analysis shows the cloud base height (CBH) of cumulus, which to a first  
 281 approximation is the same as the lifting condensation level of near surface air, is at about  
 282 650 m to 700 m with cloud tops about 160 m higher. Stratus are about 130 m thick on  
 283 average, with an average CBH between 1600 m to 1850 m. The stratiform layers that are  
 284 connected to a convective core during the time of observation have a CBH between 980 m  
 285 to 1050 m and a cloud top height between 1240 m to 1370 m, which is somewhat lower  
 286 than for Stratus.

287 Looking at single entities of the clouds detected within the classified 6 h analysis  
 288 periods, we found no evidence, that the properties of the cloud elements were influenced  
 289 by the pattern. We had imagined that stratiform clouds formed by *Gravel* might form  
 290 more from convective outflow, and those forming in *Flowers* may form more in-situ, so  
 291 that the stratiform cloud elements they incorporate would differ. To the extent such dif-  
 292 ferences exist they were not detectable. What this means is that independent of the meso-  
 293 scale organization, a stratiform layer, when it forms, has similar macro-physical prop-  
 294 erties across patterns e.g., for both *Flowers* and *Sugar*. The only differences are that it  
 295 occurs more rarely for *Sugar* and that the size of the stratiform components ("StSc"; "StSc+Cu")  
 296 increases from *Sugar* (24 km; 56 km) via *Gravel* (30 km; 84 km) to *Fish* (32 km; 181 km  
 297 and *Flowers* (47 km; 151 km)). The average of the upper 5th percentile is given in brack-  
 298 ets for the two stratiform categories as this can be assumed to better capture the char-  
 299 acteristic length of the stratiform cloud decks by excluding very small entities and en-  
 300 tities whose path length is much smaller than the actual characteristic length as clouds  
 301 rarely drift over the observatory with the latter. The measurement time has been trans-  
 302 lated into length by assuming a mean wind speed of  $10 \text{ m s}^{-1}$  at cloud top.

303 As an alternative way to look for the signature of different cloud-controlling pro-  
 304 cesses, Fig. 4 presents a Contoured Frequency by Altitude Diagram (CFAD) for the dif-  
 305 ferent patterns. It thus illustrates the frequency of occurrence of a specific reflectivity  
 306 at a certain height composited on different patterns.

307 Some features can be identified across multiple patterns. For instance an arc-like  
 308 mode, extending upward from low-reflectivities ( $-30 \text{ dBZ}$ ) near cloud base (0.7 km) to-  
 309 ward higher reflectivities (15 dBZ) at about 2 km is identified with the imprint of the non-  
 310 precipitating cumulus humilis (Lonitz et al., 2015). These can be found across all pat-

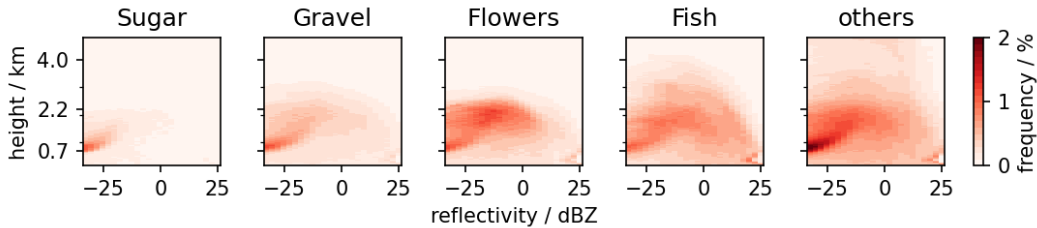


**Figure 4.** Contoured frequency by altitude diagram (CFAD) for the four patterns of shallow convection and less clear patterns gathered in the group *Others*. The colors indicate the frequency of occurrence of a reflectivity-height tuple within a specific pattern.

311 terns and contribute to a large extent to the total cloud cover of *Sugar* and *Gravel*, which  
 312 is about 0.3 and 0.4, respectively (Fig. 3).

313 Besides the robustness of the cloudiness near cloud-base, Fig. 4 also shows that the  
 314 vertical extent of clouds are more or less strongly capped at a particular height. *Sugar*  
 315 echoes diminish upward with very little signal at the expected top of the moist layer, *Flow-*  
 316 *ers* echoes are clearly capped at about 2.2 km. *Fish* echoes and *Others* frequently ex-  
 317 tend to 3 km and deeper with little evidence of strong capping.

318 The capping is not the only difference between *Flowers* and *Fish*. Despite a sim-  
 319 ilar cloud cover of about 0.5, the stratiform layer differs in these cases. Whereas *Flow-*  
 320 *ers* show a second distinct reflectivity maximum at about 2.2 km and near  $-5$  dBZ, the  
 321 distribution is more monomodal for *Fish*. This two-layer structure suggests that *Flow-*  
 322 *ers* are only sporadically connected by higher cumulus convection whereas for *Fish*, clouds  
 323 aloft appear to be deeper and as a more continuous extension of clouds near cloud base.  
 324 More like a more active and deeper distribution of *Gravel*. The deeper echoes for *Fish*  
 325 are also evident in a stronger precipitation feature (i.e., 25 dBZ near surface mode).

### 326 3.2 Rainfall

327 To assess, how important precipitation might be for different patterns, we charac-  
 328 terize its frequency and strength in the following. From the example time-series shown  
 329 in Fig. 2 and the results from the previous section, we expect a clear separation of the  
 330 precipitation characteristics among the patterns: from the lack of rain during the occur-

331 rence of *Sugar*, to frequent showers in the case of *Gravel*, to yet stronger rain events for  
 332 *Fish*.

333 To test this expectation, we take a look at the precipitation measurements from  
 334 the BCO within the same 6-hour time windows used in the section above. First, we quan-  
 335 tify how many analysis windows contain any rain event. With the exception of *Sugar*,  
 336 in more than 50 % of the identified cases, rain is present. For *Sugar* precipitation can  
 337 be detected in only 35 % of the cases.

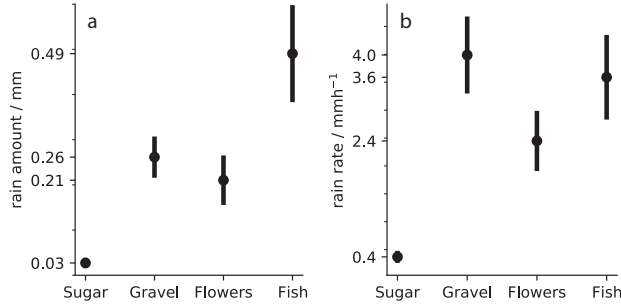


**Figure 5.** Rain statistics of each pattern averaged over a 6-hour period. The average rain amount (left) and the average maximum rain rate of each window (right) are shown with their standard error.

338 This absence of rain events in case of *Sugar* is even more evident in the quantifi-  
 339 cation of the mean near-surface rainfall (Fig. 5a). Rain amounts are similar for *Flow-*  
 340 *ers* and *Gravel*, consistent with the frequency of near surface echoes evident in Figs. 3  
 341 and 4, nearly twice as large for *Fish*. We also quantify rain intensity by averaging the  
 342 maximum rain-rates within each analysis window for each of the patterns. Among the  
 343 precipitating patterns rain intensities do not differ as substantially. In all of these cases  
 344 the precipitation is intense (approach 10 cm a day), and well above the threshold ( $1 \text{ mm h}^{-1}$   
 345 to  $2 \text{ mm h}^{-1}$ ) that past studies have associated with the formation of cold-pools (Barnes  
 346 & Garstang, 1982; Drager & van den Heever, 2017).

347 By applying the threshold of  $1 \text{ mm h}^{-1}$  to the maximum rain events, the number  
 348 of cases with significant rainfall decreases to 12 % in case of *Sugar* and about 35 % for  
 349 the other patterns. 35 % might not seem to be a lot, but it has to be kept in mind, that  
 350 these patterns are of meso-scale extent and even a 6 h-period cannot capture the com-  
 351 plete variability. This is especially the case for the *Fish* pattern, where a 6 h-period might

352 only capture the clear-sky part of the *Fish* and therefore the importance of precipita-  
 353 tion can be underestimated for a single 6 h-period, especially under the assumption, that  
 354 the clear-sky part depends on the dynamics in the cloudy part and cannot exist inde-  
 355 pendently. *Sugar*, *Gravel* and *Flowers* all consist of several individual cloud patches, while  
 356 *Fish* is often occurring as a single, large-scale network of clouds that can be separated  
 357 by its equally characteristic wide-spread clear-sky areas by several hundreds of kilome-  
 358 ters.

359 Our data does not contain sufficient samples to evaluate to what extent the spatio-  
 360 temporal characteristics of precipitation differs among the patterns. However, by analysing  
 361 the precipitation signature in all 138 6-hourly windows of *Fish*, there is evidence of a bi-  
 362 modal distribution of rain events, with a second mode consisting of extended periods of  
 363 precipitation (like the one shown in Fig. 2) that is not evident for either the case of *Flow-*  
 364 *ers* or *Gravel*.

365 Overall, precipitation events of significant strength occur during *Gravel*, *Flowers*  
 366 and *Fish* periods and suggest to play a role in the patterning process or at least in the  
 367 persistence of these patterns. There is no hint that precipitation is important for *Sugar*.  
 368 To understand why these patterns are occurring in the first place, we take a look at the  
 369 atmospheric environment these patterns go along with in the next section.

## 370 4 Meteorological environment

371 In the previous section we characterized similarities and differences in cloud- and  
 372 precipitation-signatures among the four patterns. Presumable differences among patterns  
 373 are not simply a random selection of different states of self-organization. To the extent  
 374 the patterns are forced, this forcing might be evident in the local meteorological setting,  
 375 or as a transient response to the adjustment from different upstream environments. In  
 376 this section, we address the first possibility and investigate the meteorological settings,  
 377 first at the surface and then within the free troposphere, for the different patterns.

### 378 4.1 Surface measurements

379 Near surface (5 m and 25 m above mean sea level) meteorological measurements at  
 380 the BCO are composited by pattern in Fig. 6. Common to all variables shown is a dis-  
 381 tinguished value for at least one of the patterns.

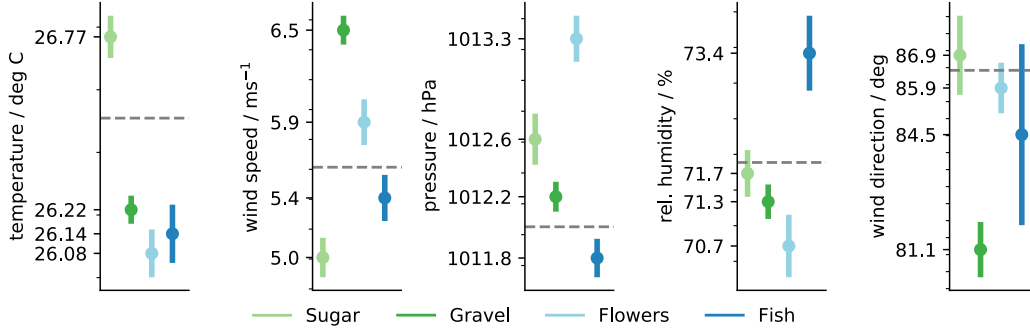


**Figure 6.** Surface meteorology measured at the BCO during the observation of the four patterns. The seasonal mean of the observed time-period independent of any pattern is drawn as grey line.

382 *Sugar* distinguishes itself from other patterns by virtue of its mean temperature  
 383 and low wind-speed. Given that annual cycle of surface temperatures is just over 2 K this  
 384 0.6 K difference is large. While *Sugar* is associated with unseasonably warm conditions,  
 385 the contrast with the other patterns is due in equal part to them being unseasonably cool,  
 386 which is consistent with *Sugar* arising during periods with little northerly contribution  
 387 to the mean flow. *Gravel* is distinguished by the surface winds being unseasonably strong  
 388 and northerly. *Flowers* are found on the days that are coolest, when surface winds are  
 389 strong, but not so strong as for *Gravel*, and when the surface pressure is unseasonably  
 390 high (1013.3 hPa). In contrast *Fish* which are also associated with extensive cloud cov-  
 391 erage (Fig. 3) are found on days with unseasonably low pressure (1011.8 hPa), high hu-  
 392 midity and relatively low but quite variable (in terms of direction) winds, consistent with  
 393 more disturbed conditions and extended periods of precipitation.

394 Amongst all analyzed surface observations, wind speed is the best proxy for a spe-  
 395 cific pattern. The lowest mean wind is measured during *Sugar* situations with  $5 \text{ m s}^{-1}$ .  
 396 For the other patterns the mean wind speed increases by an increment of  $0.5 \text{ m s}^{-1}$  from  
 397 *Fish* to *Flowers* to *Gravel*. The finding that *Flowers* and *Gravel* occur in conditions of  
 398 higher winds is consistent with what was found by Bony et al. (2020), but further dis-  
 399 discriminates among all patterns rather than two groupings (e.g., *Flowers* and *Gravel* as  
 400 high wind-speed and *Sugar* and *Fish* as low wind-speed patterns). We gain similar re-  
 401 sults to Bony et al. (2020) when compositing the ERA5 surface data (Fig. S1). On the  
 402 one hand, this finding is indicative that the different methods to detect the meso-scale

403 organization are in agreement, on the other hand, it also suggests that there may be pro-  
 404 cesses that are not captured by the analysis.

405 **4.2 Vertical structure**

406 In this section we extend the previous analysis in the vertical through a compos-  
 407 site analysis of the Grantley Adams radiosonde data. As compared to temperature and  
 408 humidity profiles derived from the Raman lidar at the BCO, the soundings have the ad-  
 409 vantage that they give meaningful profiles even in case of cloudy situations, where the  
 410 lidar attenuates. The radiosondes also provide wind profiles through the depth of the  
 411 troposphere (the wind lidar at the BCO mostly measured vertical wind, and then only  
 412 in the lowest 1 km). The pattern mean-soundings, and their associated uncertainty es-  
 413 timate, are presented in Fig. 7. Composites are made of the equivalent potential tem-  
 414 perature, potential temperature difference ( $\Theta - \bar{\Theta}$ , where  $\bar{\Theta}$  is the mean sounding across  
 415 all patterns), relative humidity and wind speed.

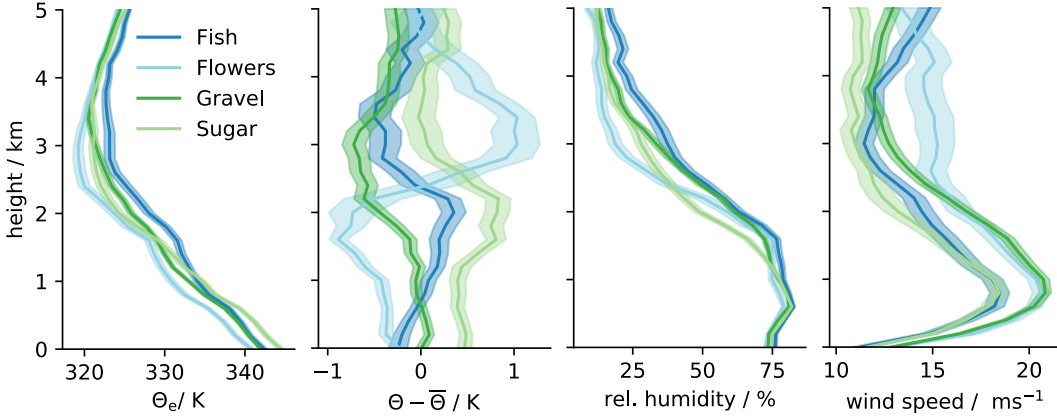


**Figure 7.** Average profiles of equivalent potential temperature, potential temperature differ-  
 416 ence to the overall pattern mean and relative humidity from soundings at the Grantley Adams  
 417 Airport.

416 Surface temperature differences measured at the BCO are also evident in the sound-  
 417 ings, and extend through the depth of the moist (lower 3 km) layer. *Flowers* distinguish  
 418 themselves not only by virtue of lower surface temperatures, but also by a much stronger  
 419 stratification atop the humid layer, showing a strong inversion at about 2.5 km. *Sugar*  
 420 appears associated with a much shallower cloud layer, also capped by an inversion. The

421 apparent instability (decrease in  $\Theta$  with height) for the other patterns simply indicates  
 422 that they are less stable on average. The lower-tropospheric stability (LTS) is  $16.2 \pm 0.3\text{K}$   
 423 in case of *Flowers* and nearly 2 K lower for *Fish* ( $14.7 \pm 0.2\text{K}$ ), *Sugar* ( $14.4 \pm 0.2\text{K}$ ) and  
 424 *Gravel* ( $14.1 \pm 0.1\text{K}$ ). However, in the case of *Sugar*, the value of  $\Theta$  at 700 hPa (which  
 425 is used to construct LTS) may miss the shallow stable layer that appears to cap the con-  
 426 vective development of this pattern.

427 The relative humidity profile is strongly coupled to the convective activity and hence  
 428 the echo fraction (e.g., Fig. 3) As we have shown in the last section, *Sugar* is mostly char-  
 429 acterized by cloudiness at cloud-base height with only few clouds reaching up to 1.8 km.  
 430 In agreement, the according moisture profile shows a shallower layer compared to the  
 431 other patterns that more regularly reach the inversion height and distribute moisture.  
 432 Likewise *Fish*, with echos reaching much more deeply through the lower troposphere is  
 433 also considerably moister than the other patterns above 3 km. These humidity profiles  
 434 also help explain differences in  $\theta_e$ , particularly in the upper cloud layer and lower free-  
 435 troposphere. For example as seen by contrasting *Fish* and *Gravel*.

436 Based on measurements made during RICO, Nuijens et al. (2009) analyzed differ-  
 437 ences in  $\theta_e$  similar to those shown in Fig. 7. Consistent with their findings these profiles  
 438 seem to co-vary consistently with surface wind speeds. Stronger surface winds for *Gravel*  
 439 and *Flowers* are mostly confined to the moist layer for *Gravel*, but extend through the  
 440 lower troposphere for *Flowers*. These winds are one component of what is often thought  
 441 of as an externally imposed large-scale forcing, to which the boundary layer thermody-  
 442 namic profiles relatively quickly equilibrate. Other aspects of this forcing, like the lower  
 443 tropospheric stability and large-scale subsidence are examined in more detail next.

### 444 **4.3 Large-scale forcing**

445 We first examine how the large-scale subsidence ( $\omega_{500}$ ) varies as a function of pat-  
 446 tern. To better judge on which scale the forcing acts, we retrieve ERA5 data in a  $20^\circ \times$   
 447  $20^\circ$  domain centered around each classification of the neural network. Those domains  
 448 are afterwards averaged to one composite that shows the strength of subsidence at the  
 449 center of each pattern, but also in its surrounding.

450 Fig. 8 reveals, that all patterns occur during times of subsidence and that this sub-  
 451 sidence is in most cases also similar to the typical subsidence rate of  $0.05 \text{ hPa s}^{-1}$  in the

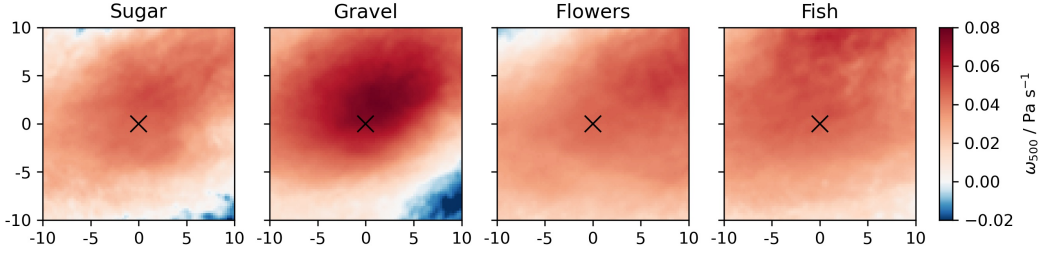


**Figure 8.** Distribution of subsidence strength  $\omega_{500}$  relative to identified pattern centers composited by 20x20 degree domains around each identified pattern. Pattern centers are marked with a cross.

452 Atlantic trade-wind regime (Holland & Rasmusson, 1973). However, it also shows that  
 453 some variability in the large-scale forcing exists and stronger subsidence is, contrary to  
 454 expectation, not occurring during *Sugar* and *Flowers* cases, but rather during *Gravel* cases  
 455 (Tab. 2).

**Table 2.** Large-scale forcing averaged by pattern from fixed-location sounding data (snd) and ERA5 data from pattern center

Pattern	LTS <sub>snd</sub>	LTS <sub>ERA5</sub>	$\omega_{500,ERA5}$	freq. of convergence
Sugar	14.4 K	14.8 K	0.046 Pa s <sup>-1</sup>	28%
Gravel	14.1 K	14.4 K	0.072 Pa s <sup>-1</sup>	38%
Flowers	16.2 K	16.6 K	0.046 Pa s <sup>-1</sup>	34%
Fish	14.7 K	16.0 K	0.048 Pa s <sup>-1</sup>	59%

456 In the subtropics, particularly in association with stratocumulus, subsidence co-  
 457 varies positively with LTS. On shorter time scales and deeper in the tropics, other fac-  
 458 tors may play a role. In particular the temperatures above the cloud layer are more tightly  
 459 coupled to moisture, so as to homogenize the density temperature on isobaric surfaces.  
 460 This partly explains the stronger temperature inversion for *Flowers*. It also means that  
 461 boundary layer variability may play a more important role in determining the LTS, con-  
 462 sistent with near-surface temperature differences as illustrated in Fig. 6. These in turn  
 463 may be influenced by the upstream conditions that the patterns sample, something we  
 464 explore with the aid of back-trajectories in the next section.

## 5 Are the four patterns indicative of specific air masses?

The four patterns occur preferentially in atmospheric conditions intrinsic to the maritime trade-wind regions.

Rasp et al. (2020) showed that globally, the four patterns predominate in the dry tropics, regions often associated with the trade winds. The analysis in the previous section identified subtle differences in the environments in which the four patterns form. This raises the question as to the origin of these environmental differences, i.e., to what extent they arise from subtle variations within the trades, or what one might alternatively think of as disturbances to or departures from canonical trade-wind conditions. We explore this question by analysing the seasonal cycle of the four patterns within our North Atlantic study region as well as the air-mass histories of the different patterns by compositing reanalysis data along back-trajectories constructed from that same data.

### 5.1 Seasonality

Seasonality is investigated using 10 years of MODIS AQUA daytime overpasses (2010–2020). The neural network classification is applied over the Tropical and North Atlantic, the results of which (Fig. 9) are presented in the form of spatial histograms of occurrence for each pattern for three seasons.

Considering just the region of the downstream trades, taken to be the tropical North Atlantic west of  $45^\circ\text{W}$ , all four patterns prevail. With the exception of *Sugar*, the absence of the four patterns in this region in other seasons supports their association with the winter trades. *Fish* and *Gravel* seem only to occur in this region in conditions (DJF) when the trades are well developed. *Flowers* are also identified in the upstream trades, increasingly so in boreal spring and early summer (AMJ). *Sugar* shows very little seasonality. Rather, and consistent with the analysis by Rasp et al. (2020), it appears associated with suppressed conditions bordering the ITCZ whose seasonal migration it follows. Based on this we hesitate to call *Sugar* a trade-wind cloud pattern.

*Flowers* are even more common in the ‘upper’ trades (east of  $45^\circ\text{W}$ ), even more so in the April–June period, (e.g., Fig. 9). Such a distribution is consistent with an affinity for conditions that favor stratocumulus. This distribution is in agreement with the analysis in the previous section, which showed that *Flowers* favor conditions of higher

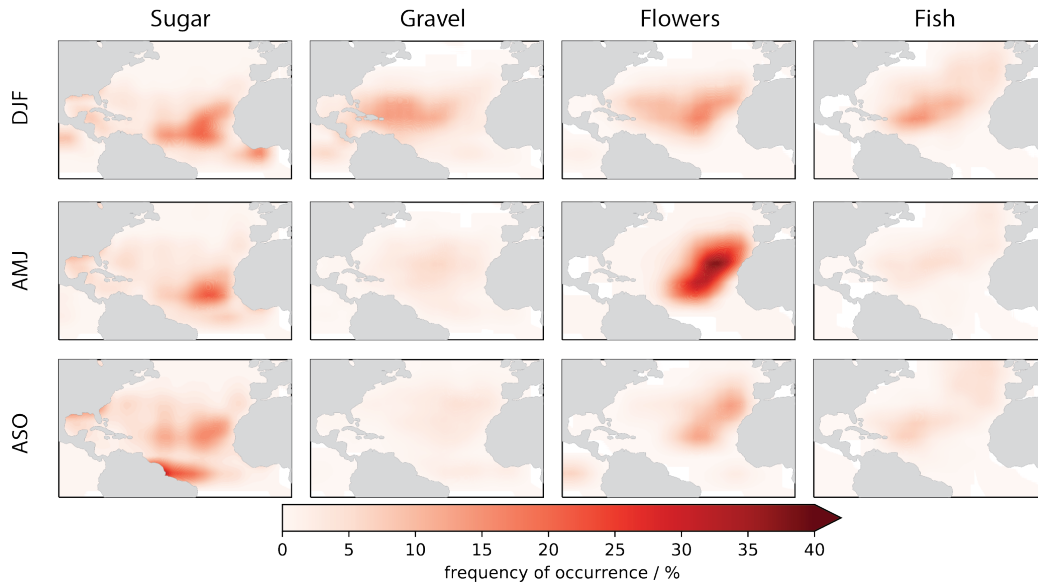


**Figure 9.** Seasonal distribution of patterns in the North Atlantic in the dry- (DJF), transitional- (AMJ) and wet- (ASO) season (top to bottom) detected in infrared imagery (AQUA MODIS 2010-2020).

495 lower tropospheric stability, and lower surface temperatures, as compared to the other  
 496 patterns. This supports the idea that *Flowers* are the downstream manifestation of the  
 497 familiar, but much smaller, closed cellular stratocumulus (Stevens et al., 2020); alterna-  
 498 tively, it may be indicative of a failing of the neural network to distinguish between *Flow-*  
 499 *ers* and closed-cells.

500 The strong association of *Flowers*, *Fish* and *Gravel* with the down-stream trades  
 501 in winter (when they are most developed), suggests that the origin of their differing en-  
 502 vironmental conditions may have less to do with the intrusion of different regimes, and  
 503 more to do with the nuanced evolution of the winter trades.

## 504 5.2 Lagrangian evolution of air masses by meso-scale organization

505 Here we use the back-trajectories, initialized at the center of the classifications fol-  
 506 lowing the boundary layer winds at 925 hPa for 84 h, to investigate possible reasons for  
 507 the environmental differences associated with each pattern.

508 Fig. 10 shows that the back-trajectories are consistent with the steadiness that char-  
 509 acterizes the winter trades, with the trajectories aligning well along the general flow of

510 the trades as they come to their point of initialization. They do however differentiate  
 511 themselves as one follows their history back in time. Most notably *Fish* which originates  
 512 far to the west of the other trajectories. A more tropical influence on *Sugar*, is also con-  
 513 sistent with its back-trajectories which start furthest south.

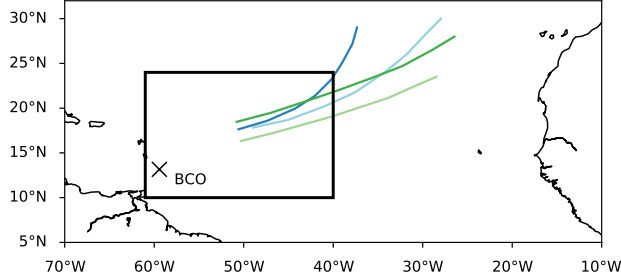


**Figure 10.** Mean back-trajectories for the different patterns initialized at the center of individual classifications within the indicated black box at 925 hPa and calculated for 84 h.

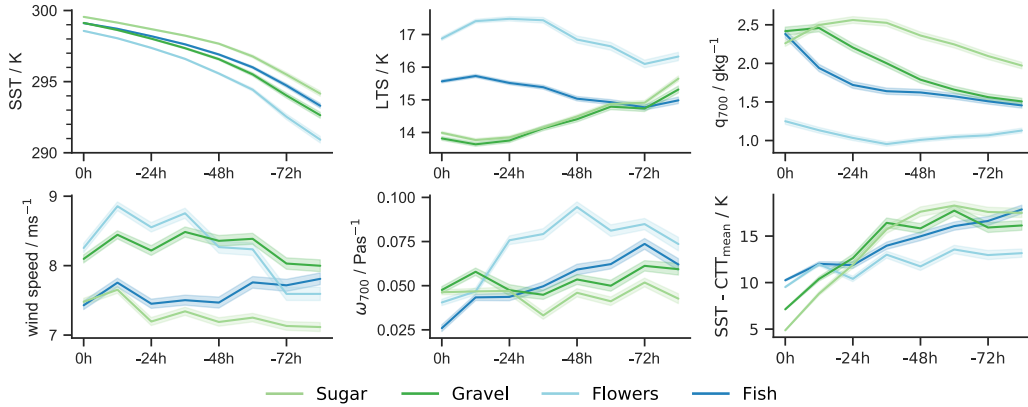


**Figure 11.** Environmental conditions along the back-trajectory. All values are ERA5 reanalysis properties, except the cloud top height estimate where the cloud top temperature (CTT) is sourced from MODIS AQUA observations. Shading indicates standard error.

514 Compositing the large-scale conditions, as given by the ERA5 reanalysis products,  
 515 along the trajectories yields further insight into factors influencing the environmental con-  
 516 ditions associated with each of the four patterns. This analysis is presented in Fig. 11.

517 This analysis is largely consistent with what was shown in the previous section, and  
 518 furthermore shows that many of the environmental differences previously documented  
 519 are apparent well in advance (and upstream) of where the pattern was eventually iden-

520 tified. *Sugar* has warmer sea-surface temperatures, weaker winds and a relatively moist  
 521 free-troposphere along its entire back-trajectory, consistent with a more tropical influ-  
 522 ence. *Flowers* evolve over cold ocean temperatures throughout the trajectory paired with  
 523 persistently high LTS (despite rising SSTs), a dry free troposphere and stronger low-level  
 524 winds. And differences in LTS among the patterns are robust and in place already 48 h  
 525 earlier.

526 The time-evolution of different fields is also indicative of dynamic influences. For  
 527 instance, for *Flowers* an acceleration of the low-level winds between  $-24$  h to  $-84$  h may  
 528 be driving the strong subsidence at 700 hPa, which in turn would support the anoma-  
 529 lously dry free-troposphere and high LTS. This pattern preceding process may drive the  
 530 differences between *Flowers* from *Gravel* with the slight slackening of the winds and the  
 531 decrease of the subsidence nearer the time and place where the pattern is identified, play-  
 532 ing less of a role. In contrast, for *Fish* a strong temporal evolution within the last 24 h,  
 533 as manifested by a pronounced moistening of the lower troposphere, might be indicative  
 534 of a dynamic disturbance. *Sugar* seems less representative of a sudden stilling in the winds  
 535 in association with *local* suppression, if anything recovering from more suppressed con-  
 536 ditions and weaker winds upstream.

537 The time-evolution of cloud top height, estimated as the difference between the ERA5  
 538 sea surface temperature and the mean cloud top temperature sourced from MODIS within  
 539 100 km around the trajectory sampling point, can further be an indication of different  
 540 lifetimes of the patterns. *Sugar* and *Gravel* seem to set up only shortly before the de-  
 541 tection ( $-36$ h) when the cloud top height dropped quickly, which would be indicative of  
 542 a shorter lifetime. In contrast, *Flowers* and *Fish* might have persisted longer at the time  
 543 of detection because the cloud top height evolves only little. The diurnality that is pro-  
 544 nounced in a number of fields (wind speed,  $\omega_{700}$ , SST-CTT) is explored in more depth  
 545 by Vial et al. (submitted).

546 In the following, we explore the idea that *Fish* is more disturbance driven with the  
 547 help of a case study.

### 548 **5.3 Extra-tropical disturbances**

549 Although we focus on the northern hemispheric winter season where the trades are  
 550 well formed, disturbances to the trade-wind mean flow are well documented (Bunker et

551 al., 1949; Riehl, 1945). The earlier literature identifies two types of disturbances, one as-  
 552 sociated with anomalously deep easterlies (which might be associated with active deep  
 553 convection), the other associated with extra-tropical intrusions in the form of trailing  
 554 cold-fronts from extra-tropical cyclones.

555 The older literature conceptualized the later (extra-tropical intrusions) as tropi-  
 556 cal incursions of the ‘polar front’. Especially in the boreal winter, when the Intertropi-  
 557 cal Convergence Zone is further south and the Azores high is less well established, frontal  
 558 disturbances can extend equator-ward. By the time they reach the subtropics, their tem-  
 559 perature signature is muted and they become most pronounced in the form of a shear  
 560 line that separates the light easterlies from the stronger north-easterlies and remains (Riehl,  
 561 1945).

562 Such a frontal passage can be seen in the surface analysis charts e.g. in association  
 563 with a deepening cyclone over the mid-Atlantic (near 45°N and 45°W) on 25th Decem-  
 564 ber 2018. Through the course of six days the cold front, initially supported by the out-  
 565 flow of cold-continental air (a cold air outbreak) from the east-coast of North-America,  
 566 occludes upon reaching the tropics as far south as Barbados (see Fig. 12).

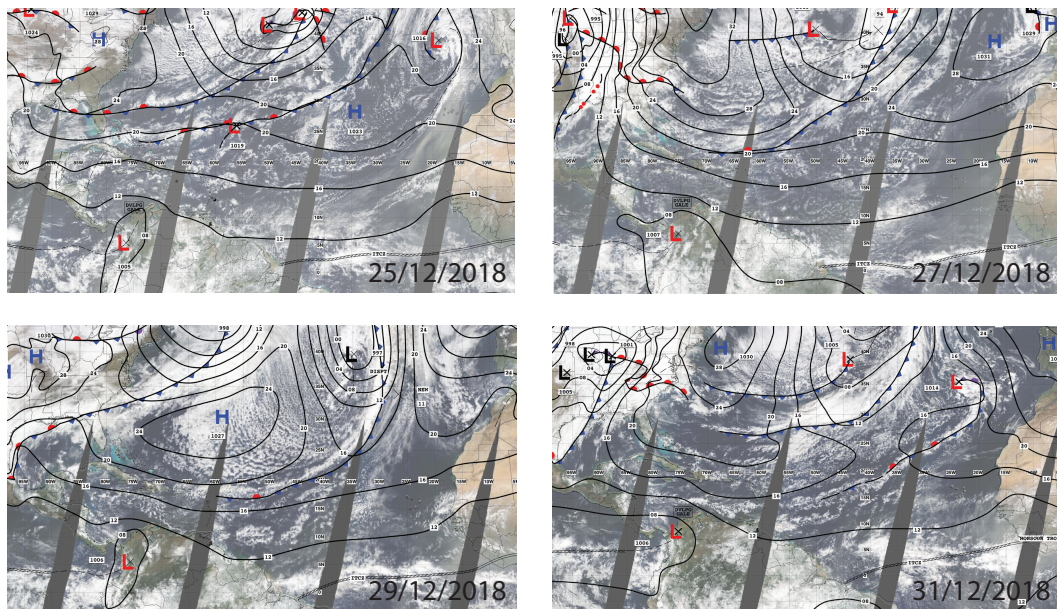


**Figure 12.** Cold air outbreak between 25th of December 2018 and 31th December 2018.

Surface analysis charts from the National Hurricane Center are adapted and overlaid on Terra MODIS images

567 By comparing the surface analysis chart with the satellite image, we recognise that  
 568 the front is visible as a band of convection that we would classify as *Fish*. In the former  
 569 cold sector, just north of the front, one can also notice on the 29th December cloud struc-  
 570 tures north of the front similar to *Flowers* (more pronounced to the west) or perhaps  
 571 *Gravel*.

572 We repeat our composite analyses done to create Fig. 8 with surface convergence  
 573 to test, whether the frontal character is typical for *Fish* and whether other patterns can  
 574 be related to the fronts as well. We find a strong signal of convergence stronger than  $-1 \times 10^{-6} \text{ s}^{-1}$   
 575 (following Weller et al. (2017)) connected with *Fish* about 60% of the identified cases  
 576 (Fig. 13). A clear signature for the other patterns is less pronounced, although the ab-  
 577 sence of convergence for *Sugar* is consistent with it being more locally suppressed. For  
 578 *Fish*, the pattern of convergence extends zonally in a way that supports the hypothesis  
 579 of *Fish* arising in association with disturbances associated with trailing cold-fronts or  
 580 shear-lines from extra-tropical intrusions.

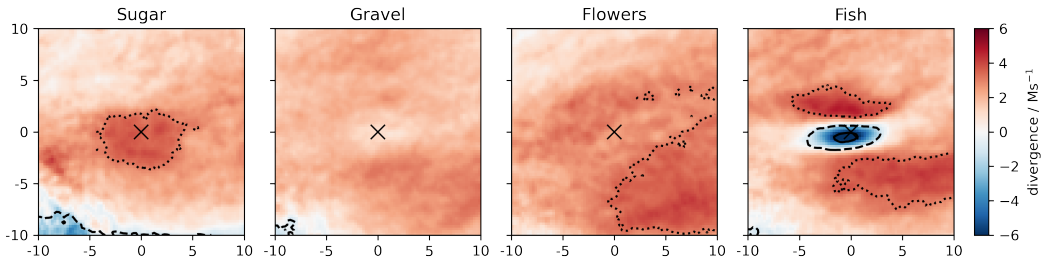


**Figure 13.** Distribution of divergence at 950 hPa relative to identified pattern centers com-  
 posed by 20x20 degree domains around each identified pattern. Counters indicate frequency of  
 events with convergence larger  $-1 \times 10^{-6} \text{ s}^{-1}$  (30%: dotted, 45%: dashed, 60%: solid). Pattern  
 centers are marked with a cross.

## 581 6 Discussion and conclusion

582 Cloud- and environmental properties associated with four patterns of meso-scale  
 583 organization in the lower trades (50°W to 60°W) of the North Atlantic are examined.  
 584 The four patterns follow the *Sugar*, *Gravel*, *Fish*, *Flowers* taxonomy of Stevens et al.  
 585 (2020) and are identified using a neural-network applied to high-resolution infra-red im-  
 586 agery from the GOES16 satellite.

587 We conditioned surface observations, back-trajectories, and reanalysis data on the  
 588 identification of different patterns to answer three questions: One, do the four patterns  
 589 show physical differences in the cloud macro-physical properties as seen by surface based  
 590 remote sensing? Two, can differences in the large-scale environment associated with dif-  
 591 ferent patterns be discerned? And, three can we identify the origins of discernible en-  
 592 vironmental differences among the patterns.

593 Fig. 14 summarizes these results and illustrates, that the four patterns differ in more  
 594 than just their satellite presentation. Cloud coverage and its vertical distribution differ  
 595 and differences in the environment of different patterns are discernible. The thermody-  
 596 namic profiles in Fig. 14 show inter-pattern differences, but also intra-pattern differences  
 597 as measured by radiosondes at points whose position relative to other features within  
 598 a pattern is schematized.

599 Many preconceptions from earlier studies, either inferred from snapshots (Stevens  
 600 et al., 2020) or from compositing reanalysis data on values of a cloud-clustering index  
 601 that correlate with different patterns (Bony et al., 2020), are supported by our analy-  
 602 sis. As an example, *Flowers*, and to some extent *Fish*, have a stratiform component de-  
 603 tectable from surface-based remote sensing. In the latter this is less distinctly a capping  
 604 stratiform, or stratocumulus layer, as it is associated with more cloudiness throughout  
 605 the cloud layer. Compared to the mean conditions, or the other patterns, LTS is higher  
 606 (0.5 K to 1.0 K) for *Fish* and (2 K) for *Flowers*.

607 Non-precipitating cloud coverage at the the lifting condensation level, as empha-  
 608 sized by Nuijens et al. (2014) for the entirety of trade-wind cloudiness, also holds across  
 609 the four patterns. This came as a surprise given that *Flowers* and *Fish* are character-  
 610 ized in part by their cloud free areas. Differences in cloud-base echo fraction largely re-  
 611 flect differences in precipitation, suggesting that to the extent environmental conditions  
 612 demand an increase in the mass flux out of the subcloud layer, for instance as shown by  
 613 George et al. (2020), this is largely associated with the development of deeper clouds and  
 614 precipitation.

615 Similar to what was found by (Bony et al., 2020), near surface winds identify *Flow-*  
 616 *ers* and *Gravel* with strong near-surface winds, and *Fish* and *Sugar* with light winds.  
 617 Our analysis, further discriminates within these two groups, with *Sugar*, *Fish*, *Flowers*  
 618 and *Gravel* each being separated by a roughly  $0.5 \text{ m s}^{-1}$  increase in surface wind speeds.

619 Precipitation increases with near surface winds, as previously noted for measurements  
 620 during RICO (Nuijens et al., 2009), with *Fish* being an outlier whose large rain rates are  
 621 associated with extra-tropical disturbances and anomalous low-level convergence.

622 Seasonal variations and back-trajectories provide further insight into the origin of  
 623 differences in the environments of the different patterns. The view of trade-wind clouds  
 624 as cumulus humilis, and hence non-precipitating with little vertical extent, as popular-  
 625 ized by studies based on data from BOMEX (Siebesma & Cuijpers, 1995) and most closely  
 626 associated with *Sugar* suggests that these are rather uncharacteristic of the trades. *Sugar*  
 627 is found to favor more suppressed conditions, uncharacteristically (for the trades) weak  
 628 winds, and proximity to deeper convection in the ITCZ.

629 As a historical note, the third author recalls that when the large-eddy simulation  
 630 community began focusing on shallow trade-wind convection through simulations of con-  
 631 ditions derived from BOMEX data (Siebesma et al., 2003), Bruce Albrecht admonished  
 632 us that less suppressed and more stratiform capped conditions – as for instance seen and  
 633 simulated in association with the Atlantic Trade-Wind Experiment (Stevens et al., 2001,  
 634 ATEX) and which we might today call *Flowers*– were more characteristic of the Trades.  
 635 We find confirmation for his point of view, twenty years later, in our data. Given the as-  
 636 sociation of *Fish* with shear lines from remnant extra-tropical cold fronts intruding deep  
 637 into the sub-tropics, only *Gravel* is left to add to *Flowers* as an archetypical form of trade-  
 638 wind convection. *Fish* and *Sugar* are intruders.

639 *Gravel* and *Flowers* differ substantially in their cloud amounts (as seen here) and  
 640 their cloud radiative effects, as shown by Bony et al. (2020). Our analysis suggests that  
 641 this difference can be attributed to slightly weaker winds, and a substantially warmer  
 642 and drier free-troposphere in the case of *Flowers*. This supports the development of a  
 643 stronger capping inversion, and stronger boundary layer cooling. Based on back-trajectories  
 644 we hypothesize that these conditions arise from an acceleration of the trades and stronger  
 645 subsidence in the upstream flow along *Flowers* back-trajectories. This hypothesis lends  
 646 itself well to tests with LES, and may even be evident at the somewhat coarser resolu-  
 647 tion now being simulated by a new generation of global storm-resolving models.

648 Independent of the formation mechanism, understanding of the conditions favor-  
 649 ing one or the other pattern may help anticipate to what extent climate change, by virtue  
 650 of changes in wind-speeds, or the frequency of extra-tropical disturbances, or changes

651 in the opacity and stability of the free troposphere, will color the frequency of different  
652 patterns, and thus cloud-radiative effects in the lower trades.

### 653 **Open Research**

654 Primary data and scripts used in the analysis and other supplementary informa-  
655 tion that may be useful in reproducing the authors' work can be obtained from 10.5281/  
656 zenodo.4432542. The ERA5 datasets used in this study (Hersbach, H. et al., 2018a, 2018b)  
657 have been provided by the Climate Data Store. GOES-16 Advanced Baseline Imager Level  
658 1b Radiances are available at <https://doi.org/10.7289/V5BV7DSR>. MODIS imagery  
659 originates from the NASA Worldview application ([https://worldview.earthdata.nasa](https://worldview.earthdata.nasa.gov)  
660 [.gov](https://worldview.earthdata.nasa.gov)), part of the NASA Earth Observing System Data and Information System (EOS-  
661 DIS).

### 662 **Acknowledgments**

663 We thank the members of the Tropical Cloud Observation group for maintaining the Bar-  
664 bados Cloud Observatory and fruitful discussions. We would also like to thank Jiawei  
665 Bao for helpful comments on an earlier version of this manuscript.

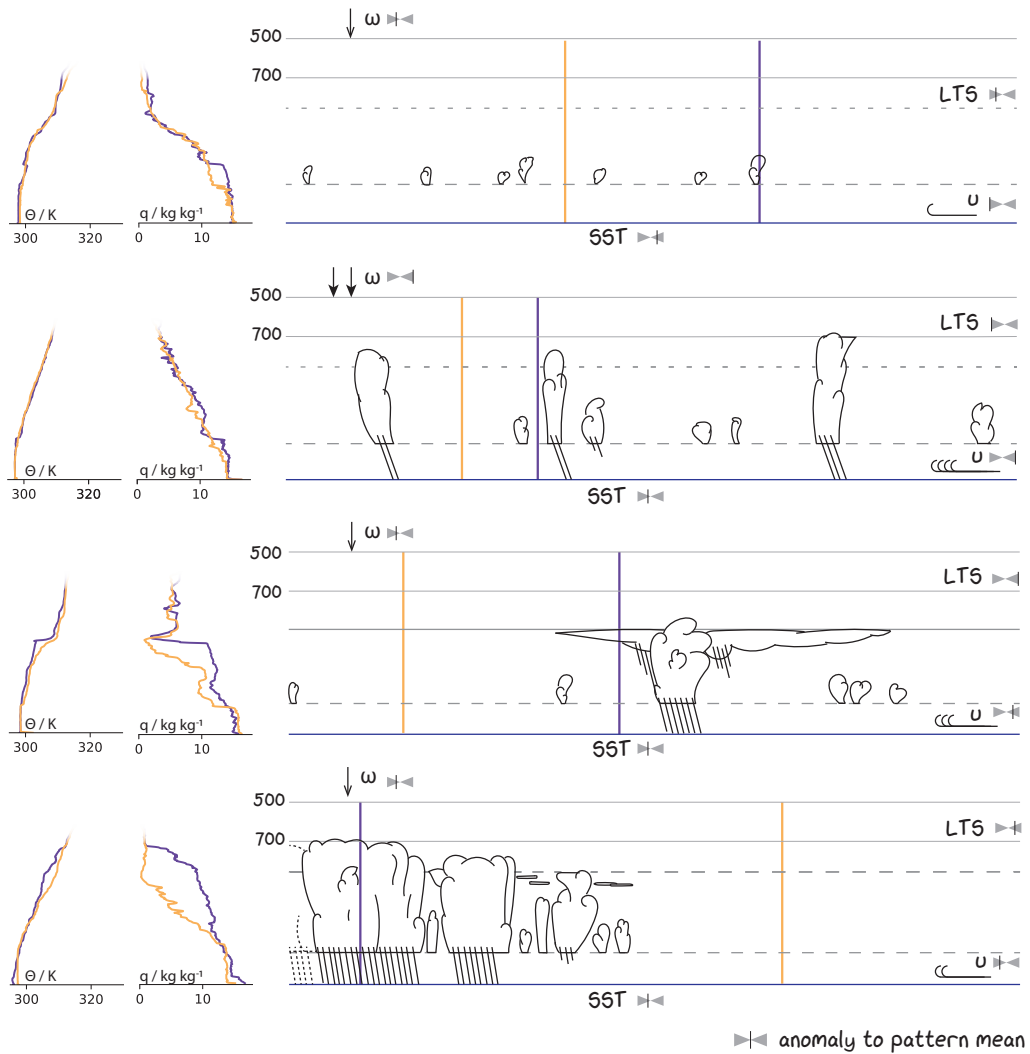


**Figure 14.** Illustration of the cloud field during the four patterns of meso-scale organization and the associated large-scale forcing (right) including the thermodynamic profiles (left). The anomaly in forcing to the pattern mean is indicated by grey sliders. Vertical lines indicate the contrasting positions of the thermodynamic profiles, purple being in the moist part and orange in the dry area. Thermodynamic profiles are based on soundings during the EUREC<sup>4</sup>A field campaign (Stephan et al., 2020)

666 **References**

- 667 Agee, E. M. (1987, January). Mesoscale cellular convection over the oceans. *Dynam-*  
 668 *ics of Atmospheres and Oceans*, *10*(4), 317–341. doi: 10.1016/0377-0265(87)  
 669 90023-6
- 670 Atkinson B. W., & Wu Zhang J. (1996, November). Mesoscale shallow convection  
 671 in the atmosphere. *Reviews of Geophysics*, *34*(4), 403–431. doi: 10.1029/  
 672 96RG02623
- 673 Barnes, G. M., & Garstang, M. (1982, February). Subcloud Layer Energetics of Pre-  
 674 cipitating Convection. *Monthly Weather Review*, *110*(2), 102–117. doi: 10  
 675 .1175/1520-0493(1982)110<0102:SLEOPC>2.0.CO;2
- 676 Bony, S., & Dufresne, J.-L. (2005). Marine boundary layer clouds at the heart of  
 677 tropical cloud feedback uncertainties in climate models. *Geophysical Research*  
 678 *Letters*, *32*(20), n/a–n/a. doi: 10.1029/2005GL023851
- 679 Bony, S., Schulz, H., Vial, J., & Stevens, B. (2020). Sugar, Gravel, Fish, and  
 680 Flowers: Dependence of Mesoscale Patterns of Trade-Wind Clouds on Environ-  
 681 mental Conditions. *Geophysical Research Letters*, *47*(7), e2019GL085988. doi:  
 682 10.1029/2019GL085988
- 683 Bunker, A. F., Haurwitz, B., Bernhard, Malkus, Joanne Starr, & Stommel, Henry  
 684 M. (1949). Vertical distribution of temperature and humidity over the  
 685 Caribbean Sea. *PAPERS IN PHYSICAL OCEANOGRAPHY AND ME-*  
 686 *TEOROLOGY*, *11*(1), 82.
- 687 Drager, A. J., & van den Heever, S. C. (2017). Characterizing convective cold  
 688 pools. *Journal of Advances in Modeling Earth Systems*, *9*(2), 1091–1115. doi:  
 689 10.1002/2016MS000788
- 690 Eastman, R., & Wood, R. (2016, January). Factors Controlling Low-Cloud Evolu-  
 691 tion over the Eastern Subtropical Oceans: A Lagrangian Perspective Using the  
 692 A-Train Satellites. *Journal of the Atmospheric Sciences*, *73*(1), 331–351. doi:  
 693 10.1175/JAS-D-15-0193.1
- 694 George, G., Stevens, B., Bony, S., Klingebiel, M., & Vogel, R. (2020). Observed im-  
 695 pact of meso-scale vertical motion on cloudiness. *J. Atmos. Sci.*, 1–30.
- 696 Hersbach, H., Bell, B., Berrisford, P., Hirahara, S., Horányi, A., Muñoz-Sabater, J.,  
 697 ... Thépaut, J.-N. (2020). The ERA5 global reanalysis. *Quarterly Journal of*  
 698 *the Royal Meteorological Society*, *146*(730), 1999–2049. doi: 10.1002/qj.3803

- 699 Hersbach, H., Bell, B., Berrisford, P., Biavati, G., Horányi, A., Muñoz Sabater, J.,  
700 ... Thépaut, J-N. (2018a). *ERA5 hourly data on pressure levels from 1979 to*  
701 *present*. Copernicus Climate Change Service (C3S) Climate Data Store (CDS).  
702 doi: 10.24381/cds.bd0915c6
- 703 Hersbach, H., Bell, B., Berrisford, P., Biavati, G., Horányi, A., Muñoz Sabater, J.,  
704 ... Thépaut, J-N. (2018b). *ERA5 hourly data on single levels from 1979 to*  
705 *present*. Copernicus Climate Change Service (C3S) Climate Data Store (CDS).  
706 doi: 10.24381/cds.adbb2d47
- 707 Holland, J. Z., & Rasmusson, E. M. (1973, January). Measurements of the At-  
708 mospheric Mass, Energy, and Momentum Budgets Over a 500-Kilometer  
709 Square of Tropical Ocean. *Monthly Weather Review*, *101*(1), 44–55. doi:  
710 10.1175/1520-0493(1973)101<0044:MOTAME>2.3.CO;2
- 711 Klingebiel, M., Ghate, V. P., Naumann, A. K., Ditas, F., Pöhlker, M. L., Pöhlker,  
712 C., ... Stevens, B. (2019, February). Remote Sensing of Sea Salt Aerosol  
713 below Trade Wind Clouds. *Journal of the Atmospheric Sciences*, *76*(5), 1189–  
714 1202. doi: 10.1175/JAS-D-18-0139.1
- 715 Lamer, K., Kollias, P., & Nuijens, L. (2015, June). Observations of the variability of  
716 shallow trade wind cumulus cloudiness and mass flux. *Journal of Geophysical*  
717 *Research: Atmospheres*, *120*(12), 2014JD022950. doi: 10.1002/2014JD022950
- 718 Lonitz, K., Stevens, B., Nuijens, L., Sant, V., Hirsch, L., & Seifert, A. (2015, Decem-  
719 ber). The Signature of Aerosols and Meteorology in Long-Term Cloud Radar  
720 Observations of Trade Wind Cumuli. *Journal of the Atmospheric Sciences*,  
721 *72*(12), 4643–4659. doi: 10.1175/JAS-D-14-0348.1
- 722 Medeiros, B., & Nuijens, L. (2016, May). Clouds at Barbados are representative of  
723 clouds across the trade wind regions in observations and climate models. *Pro-*  
724 *ceedings of the National Academy of Sciences*, *113*(22), E3062-E3070. doi: 10  
725 .1073/pnas.1521494113
- 726 Nuijens, L., Serikov, I., Hirsch, L., Lonitz, K., & Stevens, B. (2014, October). The  
727 distribution and variability of low-level cloud in the North Atlantic trades.  
728 *Quarterly Journal of the Royal Meteorological Society*, *140*(684), 2364–2374.  
729 doi: 10.1002/qj.2307
- 730 Nuijens, L., Stevens, B., & Siebesma, A. P. (2009, July). The Environment of Pre-  
731 cipitating Shallow Cumulus Convection. *Journal of the Atmospheric Sciences*,

- 732           66(7), 1962–1979. doi: 10.1175/2008JAS2841.1
- 733   Nuijens, Louise, & Jakob, Christian.       (2020).       Cloudy Perspectives.       In  
734       A. P. Siebesma, B. Stevens, C. Jakob, & S. Bony (Eds.), *Clouds and Climate:  
735       Climate Science’s Greatest Challenge* (pp. 1–32).       Cambridge: Cambridge  
736       University Press. doi: 10.1017/9781107447738.002
- 737   Rasp, S., Schulz, H., Bony, S., & Stevens, B.   (2020).   Combining crowd-sourcing  
738       and deep learning to explore the meso-scale organization of shallow con-  
739       vection.       *Bulletin of the American Meteorological Society*, 1–39.   doi:  
740       10.1175/BAMS-D-19-0324.1
- 741   Rauber, R. M., Ochs, H. T., Di Girolamo, L., Göke, S., Snodgrass, E., Stevens, B.,  
742       ... Twohy, C. H.   (2007, December).   Rain in Shallow Cumulus Over the  
743       Ocean: The RICO Campaign. *Bulletin of the American Meteorological Society*,  
744       88(12), 1912–1928. doi: 10.1175/BAMS-88-12-1912
- 745   Riehl, H. (1945). *Waves in the easterlies and the polar front in the tropics: A report  
746       on research conducted at the Institute of Tropical Meteorology of the University  
747       of Chicago at the University of Puerto Rico, Rio Piedras, P.R.*   Chicago, Ill.:  
748       University of Chicago Press.
- 749   Seifert, A., & Heus, T. (2013, June). Large-eddy simulation of organized precipitat-  
750       ing trade wind cumulus clouds. *Atmos. Chem. Phys.*, 13(11), 5631–5645. doi:  
751       10.5194/acp-13-5631-2013
- 752   Seifert, A., Heus, T., Pincus, R., & Stevens, B. (2015, December). Large-eddy sim-  
753       ulation of the transient and near-equilibrium behavior of precipitating shallow  
754       convection. *Journal of Advances in Modeling Earth Systems*, 7(4), 1918–1937.  
755       doi: 10.1002/2015MS000489
- 756   Siebesma, A. P., Bretherton, C. S., Brown, A., Chlond, A., Cuxart, J., Duynkerke,  
757       P. G., ... Stevens, D. E. (2003). A Large Eddy Simulation Intercomparison  
758       Study of Shallow Cumulus Convection. *J. Atmos. Sci.*, 60, 19.
- 759   Siebesma, A. P., & Cuijpers, J. W. M. (1995, March). Evaluation of Paramet-  
760       ric Assumptions for Shallow Cumulus Convection. *Journal of the Atmo-  
761       spheric Sciences*, 52(6), 650–666.   doi: 10.1175/1520-0469(1995)052<0650:  
762       EOPAFS>2.0.CO;2
- 763   Stephan, C., Schnitt, S., Bellenger, H., Schulz, H., Szoeke, S. P. D., Acquistapace,  
764       C., ... Stevens, B. (2020). *Radiosonde measurements from the EUREC4A field*

- 765 *campaign*. AERIS. doi: 10.25326/62
- 766 Stevens, B., Ackerman, A. S., Albrecht, B. A., Brown, A. R., Chlond, A., Cuxart,  
767 J., ... Stevens, D. E. (2001, July). Simulations of Trade Wind Cumuli under  
768 a Strong Inversion. *Journal of the Atmospheric Sciences*, 58(14), 1870–1891.  
769 doi: 10.1175/1520-0469(2001)058<1870:SOTWCU>2.0.CO;2
- 770 Stevens, B., Bony, S., Brogniez, H., Hentgen, L., Hohenegger, C., Kiemle, C., ...  
771 Zuidema, P. (2020). Sugar, gravel, fish and flowers: Mesoscale cloud patterns  
772 in the trade winds. *Quarterly Journal of the Royal Meteorological Society*,  
773 146(726), 141–152. doi: 10.1002/qj.3662
- 774 Stevens, B., Farrell, D., Hirsch, L., Jansen, F., Nuijens, L., Serikov, I., ... Pros-  
775 pero, J. M. (2016, May). The Barbados Cloud Observatory: Anchor-  
776 ing Investigations of Clouds and Circulation on the Edge of the ITCZ.  
777 *Bulletin of the American Meteorological Society*, 97(5), 787–801. doi:  
778 10.1175/BAMS-D-14-00247.1
- 779 Vial, J., Vogel, R., & Schulz, H. (submitted). The role of mesoscale cloud organi-  
780 zation in the daily cycle of trade-wind cumuli. *Quarterly Journal of the Royal*  
781 *Meteorological Society*.
- 782 Weller, E., Shelton, K., Reeder, M. J., & Jakob, C. (2017, May). Precipitation As-  
783 sociated with Convergence Lines. *Journal of Climate*, 30(9), 3169–3183. doi:  
784 10.1175/JCLI-D-16-0535.1
- 785 WMO. (2017). *International cloud atlas*. World Meteorological Organization.
- 786 Young, G. S., Kristovich, D. A. R., Hjelmfelt, M. R., & Foster, R. C. (2002,  
787 July). ROLLS, STREETS, WAVES, AND MORE: A Review of Quasi-  
788 Two-Dimensional Structures in the Atmospheric Boundary Layer. *Bul-*  
789 *letin of the American Meteorological Society*, 83(7), 997–1002. doi:  
790 10.1175/1520-0477(2002)083<0997:RSWAMA>2.3.CO;2
- 791 Zuidema, P., Li, Z., Hill, R. J., Bariteau, L., Rilling, B., Fairall, C., ... Hare, J.  
792 (2012, January). On Trade Wind Cumulus Cold Pools. *Journal of the Atmo-*  
793 *spheric Sciences*, 69(1), 258–280. doi: 10.1175/JAS-D-11-0143.1